

# FIRST DETECTION OF A SUB-KPC SCALE MOLECULAR OUTFLOW IN THE STARBURST GALAXY NGC 3628

AN-LI TSAI<sup>1,2,3</sup>, SATOKI MATSUSHITA<sup>2</sup>, ALBERT K. H. KONG<sup>4</sup>, HIRONORI MATSUMOTO<sup>5</sup>, KOTARO KOHNO<sup>6,7</sup>,  
 ALTSAT@ASTRO.NCU.EDU.TW

<sup>1</sup> Graduate Institute of Astronomy, National Central University, No. 300, Jhongda Rd., Jhongli, Taoyuan 32001, Taiwan

<sup>2</sup> Institute of Astronomy and Astrophysics, Academia Sinica, P.O. Box 23-141, Taipei 10617, Taiwan

<sup>3</sup> Department of Earth Sciences, National Taiwan Normal University, No. 88, Sec. 4, Tingzhou Rd., Taipei 11677, Taiwan

<sup>4</sup> Institute of Astronomy and Department of Physics, National Tsing Hua University, No. 101, Sec. 2, Kuang-Fu Rd., Hsinchu 30013, Taiwan

<sup>5</sup> Department of Physics, Nagoya University, Furo-cho, Chikusa-ku, Nagoya, Aichi 464-8602, Japan

<sup>6</sup> Institute of Astronomy, University of Tokyo, 2-21-1 Osawa, Mitaka, Tokyo 181-0015, Japan and

<sup>7</sup> Research Center for the Early Universe, University of Tokyo, 7-3-1 Hongo, Bunkyo, Tokyo 113-0033, Japan

*Draft version March 2, 2013*

## ABSTRACT

We successfully detected a molecular outflow with a scale of 370 – 450 pc in the central region of the starburst galaxy NGC 3628 through deep CO(1-0) observations by using the Nobeyama Millimeter Array (NMA). The mass of the outflowing molecular gas is  $\sim 2.8 \times 10^7 M_{\odot}$ , and the outflow velocity is  $\sim 90 \pm 10$  km s<sup>-1</sup>. The expansion timescale of the outflow is 3.3 – 6.8 Myr, and the molecular gas mass flow rate is 4.1 – 8.5 M<sub>⊙</sub> yr<sup>-1</sup>. It requires mechanical energy of  $(1.8 - 2.8) \times 10^{54}$  erg to create this sub-kpc scale molecular outflow. In order to understand the evolution of the molecular outflow, we compare the physical properties between the molecular outflow observed from our NMA CO(1-0) data and the plasma gas from the soft X-ray emission of the Chandra X-ray Observatory (CXO) archival data. We found that the distribution between the molecular outflow and the strong plasma outflow seems to be in a similar region. In this region, the ram pressure and the thermal pressure of the plasma outflow are 10<sup>-(8-10)</sup> dyne cm<sup>-2</sup>, and the thermal pressure of molecular outflow is 10<sup>-(11-13)</sup> dyne cm<sup>-2</sup>. This implies the molecular outflow is still expanding outward. The molecular gas consumption timescale is estimated as 17 – 27 Myr, and the total starburst timescale is 20 – 34 Myr. The evolutionary parameter is 0.11 – 0.25, suggesting that the starburst activity in NGC 3628 is still in a young stage.

*Subject headings:* ISM: bubbles — ISM: jets and outflows — galaxies: individual (NGC 3628) — galaxies: ISM — galaxies: starburst

## 1. INTRODUCTION

Molecular gas consumption, mainly dominated by star formation and losing gas through outflow, plays an important role on star formation. To understand the molecular gas consumption in galaxies help us to study galaxies evolution.

Galaxies with violent star formation, especially in central nuclear region, are called starburst galaxies. They have star formation rates (SFRs) several to hundreds times higher than normal spiral galaxies. The strong star formation activities of starburst galaxies produce a large number of young and massive OB stars in a very short time. These massive stars finally end up their lifetime with supernova explosions. Therefore, vast amount of stellar winds from massive stars and supernova explosions generate huge energy and high pressure to create high velocity galactic winds, which sweep up the surrounding interstellar medium (ISM) and create galactic scale outflows or superbubbles. These scenarios have been described by several analytical models (e.g., Chevalier & Clegg 1985; McCray & Kafatos 1987; Yokoo et al. 1993), numerical simulations (e.g., Tomisaka & Ikeuchi 1988; Cooper et al. 2008), and observational results (e.g., Heckman et al. 1990; Cecil et al. 2002). Previous observations mainly focused on the warm ionized and hot

plasma outflows, such as H $\alpha$  emission observations (e.g., Armus et al. 1990; Lehnert & Heckman 1996) and soft X-ray observations (e.g., Strickland et al. 2004). However, the observations on molecular outflows or superbubbles are very rare in the past. Lack of this study will cause under-estimation on the molecular gas consumption in galaxies, and have a bias to understand the galaxies evolution in our universe.

The reasons for the rarity of molecular gas detections were mostly due to their diffuse/extended nature and poor instrumental sensitivities. Recent improvements of various instruments provide a better chance to study the molecular outflows and superbubbles in galaxies. The recent techniques to detect molecular outflows and superbubbles in galaxies can be classified as three types: (1) High-velocity CO wings to detect molecular outflows, e.g., NGC 3256 (Sakamoto et al. 2006b), Mrk 231 (Feruglio et al. 2010), M51 (Matsushita et al. 2007), NGC 1266 (Alatalo et al. 2011), and local ULIRGs (Chung et al. 2011). (2) P-cygni profile to detect molecular superbubbles, e.g., Arp 220 (Sakamoto et al. 2009), and Mrk 231 (Fisher et al. 2010). (3) Direct imaging at millimeter waveband for CO molecular outflows and superbubbles, e.g., molecular outflow in M82 (Nakai et al. 1987; Walter et al. 2002), molecular superbubble in M82 (Weiss et al. 1999; Matsushita et al. 2000, 2005), and molecular superbubbles in NGC 253 (Sakamoto et al.

2006). The first and second techniques are useful to detect outflows and superbubbles from face-on galaxies. However, it is difficult to distinguish the molecular gas of outflows/superbubbles from that of galactic disk. Therefore, we cannot have an accurate measurement on molecular gas mass losing. To solve this problem, we need to observe edge-on galaxies by using the third technique. Although this technique is time consuming, we can directly observe the morphology of molecular outflows and superbubbles, and therefore can have an accurate measurement on molecular gas mass losing.

So far, only a few molecular outflows and superbubbles in galaxies have been directly imaged by using the third technique. More observations to directly image molecular outflows and superbubbles are necessary in order to understand the general properties of these structures and their influence on starburst activities. We have been conducting detail studies of one molecular outflow and two superbubbles toward the nearby edge-on starburst galaxy NGC 2146 (Tsai et al. 2009). Here, we provide another sample, NGC 3628.

Starburst galaxy NGC 3628 is a member of the interacting Leo Triplet (Arp 317), including NGC 3627, NGC 3623, and NGC 3628. NGC 3628 is the north source in the Leo Triplet, NGC 3627 is the south one, while NGC 3623 is the southwest one. Two signatures of tidal interaction in Leo Triplet are observed in several wavebands: A plume extending  $\sim 100$  kpc from the eastern edge of NGC 3628 is detected in optical, far-infrared, and HI emission (Chromey et al. 1998); a bridge between NGC 3628 and NGC 3627 is detected in HI emission (Cole et al. 1998). These structures have been modeled by Rots (1978) and were explained as a tidal interaction between NGC 3628 and NGC 3627 about 800 Myr ago.

NGC 3628 is a nearby ( $D = 7.7$  Mpc;  $1'' = 37$  pc; Tully 1988), edge-on ( $i = 87^\circ$ ; Tully 1988), and IR luminous ( $\log L_{\text{IR}}/L_\odot = 10.25$ ; Sanders et al. 2003) galaxy. The optical image of NGC 3628 looks like a boxy shape (Chromey et al. 1998; see Figure 1). Radio observations (Condon 1982) show that NGC 3628 has a circumnuclear starburst. Besides, a large-scale galactic wind has been detected in NGC 3628. Observations with ROSAT (Dahlem et al. 1996) and Chandra X-ray Observatory (CXO) (Strickland et al. 2001, 2004) show that NGC 3628 has an asymmetric plasma bipolar outflow with  $\sim 7 - 10$  kpc scale in both north and south parts; optical H $\alpha$  observations also show that NGC 3628 has a  $\sim 10$  kpc-scale warm plasma gas outflow (Strickland et al. 2004). It is natural to expect the existence of molecular outflows or superbubbles. Irwin & Sofue (1996) claimed that their CO(1-0) Nobeyama Millimeter Array (NMA) observations detected four expanding molecular superbubbles, which are associated with the low velocity gradient ridge outside of the nuclear disk. However, no molecular outflow has been detected. Our new CO(1-0) NMA observation detect a sub-kpc scale molecular outflow for the first time. We will discuss its properties, its impact on NGC 3628, and its evolution by comparing with the CXO archival data.

## 2. OBSERVATIONS AND ARCHIVE DATA

### 2.1. NMA CO(1-0) Observations

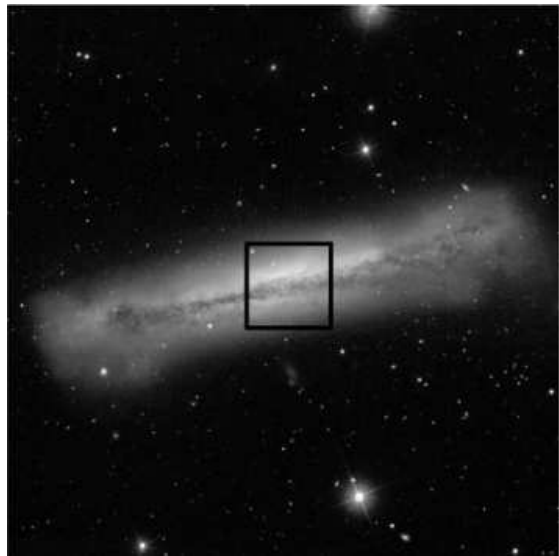


**Figure 1.** DSS Optical Image of NGC 3628. The box size is  $2' \times 2'$ , the same size of NMA CO(1-0) moment maps showing in Figure 3.

We have used the NMA to observe the CO(1-0) emission of NGC 3628 in the central  $\sim 1'$  region. The observations were made during 2000 December to 2002 February with 3 different configurations of six 10-meter antennas. The total on-source time was  $\sim 40$  hours. The phase tracking center was  $\alpha(\text{J2000}) = 11^{\text{h}}20^{\text{m}}17^{\text{s}}.011$  and  $\delta(\text{J2000}) = 13^\circ35'20''.064$ . We used tunerless SIS receivers (Sunada et al. 1994), and observed the CO(1-0) line in the upper side band. Double side band system temperature was about 200 – 300 K for most of the observations. The backend used was the XF-type spectro-correlator Ultra Wide Band Correlator (UWBC; Okumura et al. 2000), configured to have 512 MHz bandwidth with 256 channels (i.e., a 2 MHz channel width or  $5.2 \text{ km s}^{-1}$  velocity resolution). We observed 3C 273 and 3C 279 as bandpass calibrators. The phase calibrator was 1055+018, and amplitude calibrators were 1055+018, 3C 84, and 3C 345. The flux scale of 1055+018 in 2000 – 2001 was determined by comparison with Mars. That in 2001 – 2002 was determined by comparison with 3C 84 and 3C 345, which were determined by comparison with Mars, Uranus, and Neptune. The uncertainties in the absolute flux scales are estimated as 5 – 6% in 2000 – 2001 and 10 – 12% in 2001 – 2002.

The data were calibrated by using the NRO software package “UVPROC II” (Tsutsumi et al. 1997), and were CLEANed by using standard procedures implemented in the NRAO Astronomical Image Processing System (AIPS). The maps were made with natural weighting, with a final synthesized beam size of  $3''.01 \times 2''.36$  ( $147 \text{ pc} \times 115 \text{ pc}$ ), which has a higher resolution than the past CO(1-0) observations ( $3''.93 \times 2''.79$  or  $128 \text{ pc} \times 123 \text{ pc}$ ; Irwin & Sofue 1996). The position angle of the beam is  $143^\circ$ . The noise level is  $9.86 \text{ mJy beam}^{-1}$  with a velocity resolution of  $5.2 \text{ km s}^{-1}$ , better than the previous observation of Irwin & Sofue (1996),  $65 \text{ mJy beam}^{-1}$  with a velocity resolution of  $13 \text{ km s}^{-1}$ .

### 2.2. CXO Archive Data

We obtained X-ray data from the CXO archive, which were originally observed by Strickland et al. in 2000 December 2 with 60 ks total exposure time. It was observed with the Advanced CCD Imaging Spectrometer (ACIS). The nucleus of NGC 3628 is placed in the ACIS-S3 chip, which is a back illuminated CCD on the spectroscopic array. The back illuminated CCD is more sensitive to low-energy X-ray photons than the front-illuminated ACIS chips (Strickland et al. 2002; Inui et al. 2005), and therefore is powerful to observe diffuse X-ray emission in low energies, such as the X-ray superwinds. The diffuse gas images of NGC 3628 have been published in Strickland et al. (2004), but the detail properties have not yet been discussed. In order to understand the properties of the diffuse gas, such as density, mass, energy, and pressure, we reprocessed the data, extracted the spectra, and performed model fittings.

The data were reprocessed by using the Chandra Interactive Analysis of Observations software package (CIAO) version 4.2, and the Chandra Calibration Database (CALDB) version 4.2.2, released on 19 April 2010. We used the High Energy Analysis software (HEAsoft) version 6.5, and the X-Ray Spectral Fitting Package (XSPEC) version 12.4 for further analysis. The background is chosen from a source-free circular region with a radius of  $1/3$  centered at the position  $\alpha(\text{J2000}) = 11^{\text{h}}20^{\text{m}}04^{\text{s}}.86$  and  $\delta(\text{J2000}) = 13^{\circ}30'50''.49$ ,  $\sim 5'$  away from the galactic center. The background level was  $0.04 \text{ counts s}^{-1} \text{ arcmin}^{-2}$ . To avoid the bias of choosing background, we double checked with blank-sky subtraction. We used CIAO script DEFLARE and chose *sigma* as the flare-cleaning method. After clipping data with count rates less than  $3\sigma$ , the exposure time with good time intervals turned to be 56,319 s.

We only consider the data with energy between 0.3 keV and 7.0 keV. This is because the data with energy above 7.0 keV is dominated by X-ray background, and the data quality below 0.3 keV has large uncertainty due to poor calibration. We grouped the energy bins of the spectra from the selected region so that each bin would contain at least 20 counts to allow  $\chi^2$  statistics for spectral fitting. In order to analyze the diffuse and extended X-ray emission, we used two CIAO threads, WAVDETECT and CELLDetect, to detect point sources and removed them from the X-ray data. After removing detected point sources from the X-ray data, we used the CIAO thread DMFILTH to interpolate the emission at point source regions from their surrounding backgrounds.

### 3. RESULTS

#### 3.1. NMA CO(1-0) data

##### 3.1.1. Distribution

We summed every 4 channels ( $= 20.8 \text{ km s}^{-1}$ ) from the original channel maps to reduce the rms noise level. The CO(1-0) channel maps are shown in Figure 2. The noise level is  $4.93 \text{ mJy beam}^{-1}$  (68.8 mK). Comparing to the noise level of Irwin & Sofue (1996),  $65 \text{ mJy beam}^{-1}$  with a velocity resolution of  $13 \text{ km s}^{-1}$ , which corresponds to  $52 \text{ mJy beam}^{-1}$  with a velocity resolution of  $20.8 \text{ km s}^{-1}$ , the emission that Irwin & Sofue (1996) detected is  $\sim 10\sigma$  and the second contour in our Figure 2. This suggests that we could detect 10 times weaker emission than that of Irwin & Sofue (1996). The emission in each channel

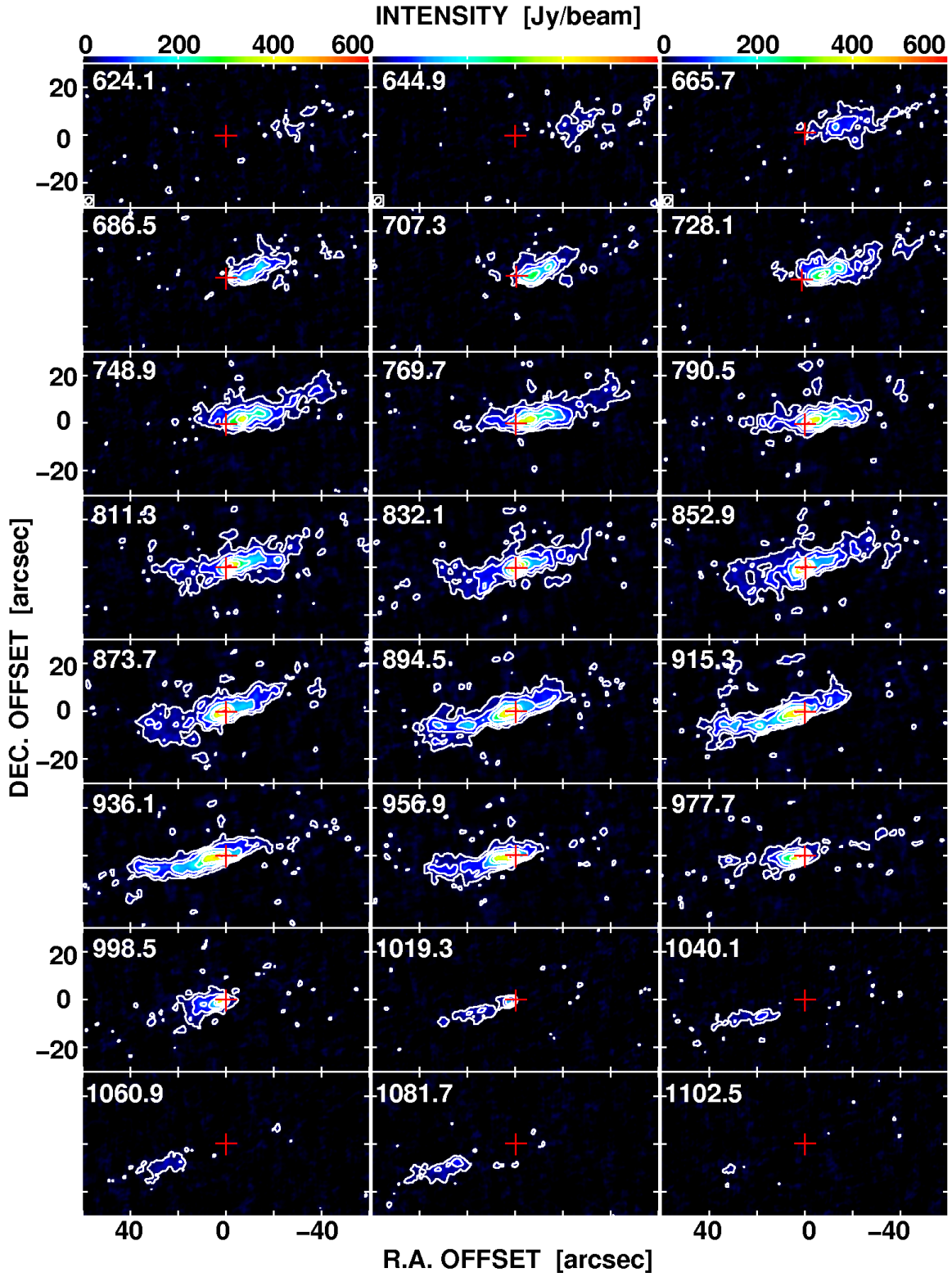
shows that most of the gas is distributed along the galactic disk, and the structure in either one or both edges of the galactic disk is fragmented. Besides, some extended diffuse features appear in the north of the galactic center in several channels.

Figure 3a is our NMA CO(1-0) integrated intensity map (moment zero map). Most of the CO emission is distributed along the galactic disk with a position angle of  $104^\circ$ . The distribution of molecular gas in the galactic disk is not symmetric with respect to the major axis. The amount of the molecular gas above the major axis is more than that below the major axis. Besides, both edges of the molecular disk are distorted. The eastern edge of the disk shows a boxy-shape structure, and the western edge of the disk is fragmented. Both edges look similar to the edges of the optical image (Figure 1) although the scale is different. An extended emission located from the center with an offset of  $(\Delta\text{R.A.}, \Delta\text{Dec.}) \sim (0'', +15'')$  labeled as *OF* is the real emission because they also appear in the same position by mapping with uniform weighting. However, those centers with position offsets of  $\sim (0'', +25'')$  and  $\sim (+7'', -20'')$  are considered as sidelobes because the positions of these features are either disappeared or shifted along with the beam patterns by mapping with uniform weighting or by choosing different UV-ranges. The existence of the strong sidelobes is due to the UV-coverage of a low-declination source, which generates strong sidelobes along the north-south direction.

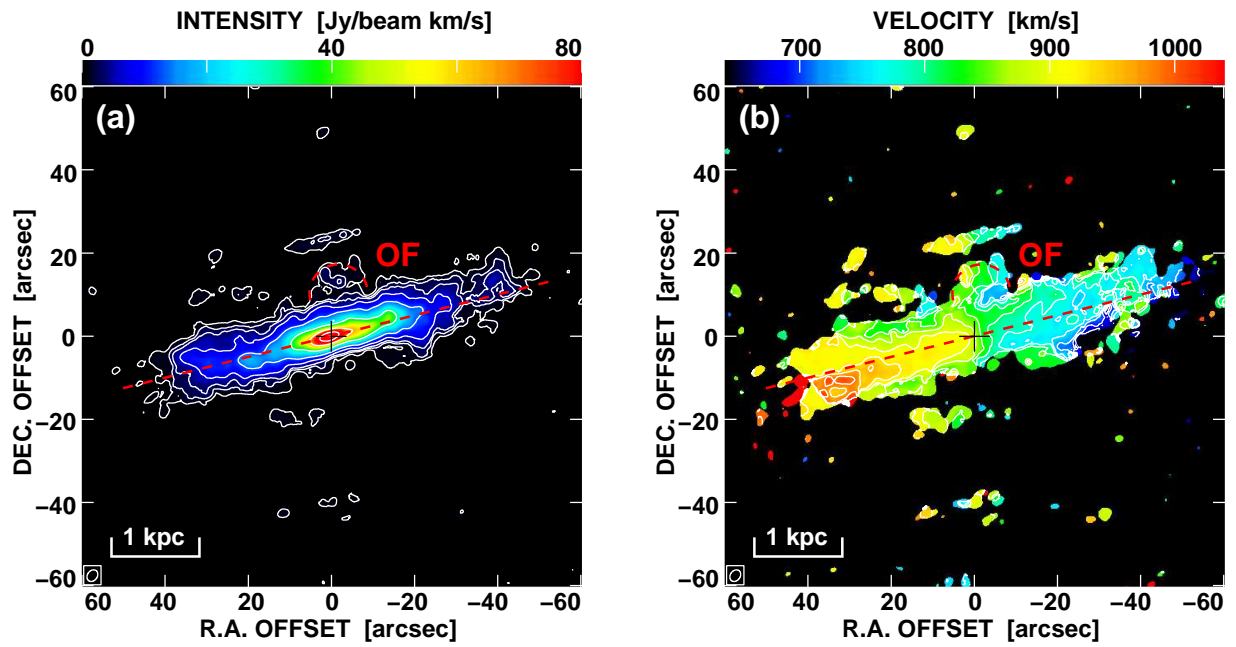
##### 3.1.2. Velocity Features

Figure 3b is the intensity weighted mean velocity map (moment one map). From this map, we can see that there is a rigid-body rotation in the galactic center and a flat rotation in larger radii in the eastern part of the disk. The velocity in the northwestern part of the disk seems to be a flat rotation, but the southwestern part of the disk does not show a clear flat rotation feature. Besides, the velocity in the western part of the disk is twisted and entangled. In order to further discuss the detail of these features, we first rotate the moment zero map until the major axis of the galactic disk is the same with the horizontal direction, namely rotating clockwise for  $14^\circ$ , as shown in Figure 4, and then we check the position-velocity (hereafter  $p-v$ ) diagrams parallel or perpendicular to the major axis.

Figure 5 shows the major-axis  $p-v$  diagram by averaging the  $p-v$  diagrams within  $2''$  (between  $+1''$  and  $-1''$  offsets) from the major-axis. From Figure 5, we found that the galactic disk consists of several structures: The curve between the position  $+60''$  and  $-60''$  indicates a rotation curve along the major axis of the galactic disk, namely, a rigid-body rotation between the positions  $+10''$  and  $-10''$ , with a flat rotation beyond these positions; this suggests the existence of a large-scale molecular gas disk. The solid line between the positions  $+4''$  and  $-4''$  indicates a rigid-body rotation, suggesting the existence of an inner molecular disk. The ellipse between the positions  $+40''$  and  $-40''$  indicates the velocity feature more or less symmetric. This feature is similar to the  $p-v$  diagram of our Galaxy (Englmaier & Gerhard 1999), suggesting the existence of a molecular bar (Binney et al. 1991; García-Burillo & Guélin 1995) in this galaxy. The solid line between the position  $+40''$  and  $-40''$  will be



**Figure 2.** NMA CO(1-0) channel maps of NGC 3628. The red cross is the phase tracking center of our observation,  $\alpha(\text{J2000}) = 11^{\text{h}}20^{\text{m}}17^{\text{s}}.011$  and  $\delta(\text{J2000}) = 13^{\circ}35'20''.064$ . The synthesizer beam size is  $3''.01 \times 2''.36$  ( $112.4 \text{ pc} \times 88.1 \text{ pc}$ ), which is shown in the lower left corner of the first panel. The contour levels are 4, 10, 20, 40, 60, 100, and  $130\sigma$ , where  $1\sigma$  is  $4.93 \text{ mJy beam}^{-1}$ . The LSR velocity, in units of  $\text{km s}^{-1}$ , is showing at the top left corner of each channel map.



**Figure 3.** The NMA CO(1-0) integrated intensity (moment zero) and intensity weighted mean velocity field (moment one) maps of NGC 3628. The cross is the phase tracking center and the synthesized beam is shown in the bottom-left corner of each map. The central position and the synthesized beam size are the same as in Figure 2. The red dashed line indicates the location of the galactic disk, and the red curve indicates the molecular outflow *OF*. (a) Moment 0 map. The contour levels are 1, 3, 5, 10, 20, 50, 100, 150, and  $180\sigma$ , where  $1\sigma$  is  $648.3 \text{ mJy beam}^{-1} \text{ km s}^{-1}$  ( $= 9.05 \text{ K km s}^{-1}$ ). (b) Moment 1 map. The contour levels are from 640, 660, 680, ..., and  $1,040 \text{ km s}^{-1}$ , increasing with  $20 \text{ km s}^{-1}$ .

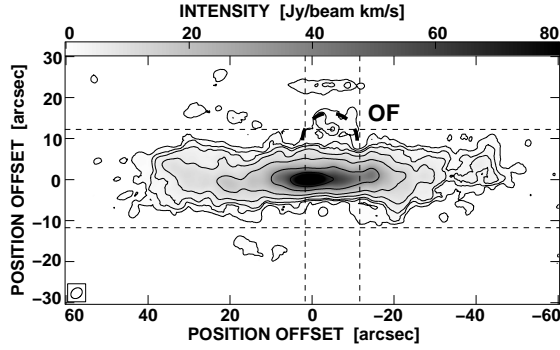


**Figure 4.** NMA CO(1-0) moment zero map after clockwise rotation of  $14^\circ$ . The contour levels are the same as in figure 3a. The two horizontal dashed lines, offset by  $+12''$  and  $-12''$  from the major axis, specify the range of major-axis  $p-v$  diagrams shown in Figure 6. The two vertical dashed lines, offset by  $+1''$  and  $-11''$  from the minor axis specify the range of  $OF$ . Its minor-axis  $p-v$  diagram is shown in Figure 7.

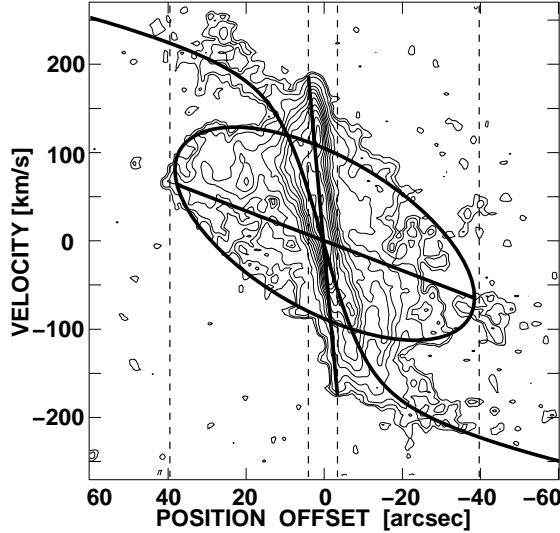


**Figure 5.** The  $p-v$  diagram along the major axis by averaging the data between the positions  $-1''$  and  $+1''$  from the major axis. The zero velocity corresponds to the systemic velocity of  $840 \text{ km s}^{-1}$ . The contour levels are 2, 3, 5, 10, 15, 20, ..., and  $50\sigma$ , where  $1\sigma$  is  $9.09 \text{ mJy beam}^{-1}$ . The solid curve between  $+60''$  and  $-60''$  indicates the rotation curve of the galactic disk. The solid line between two dashed vertical lines at  $+4''$  and  $-4''$  indicates the steep velocity gradient of the inner molecular disk. The solid line between two dashed vertical lines at  $+40''$  and  $-40''$  indicates the low velocity gradient of the outer molecular disk. The solid ellipse indicates the velocity feature of the molecular gas bar.

discussed in the following paragraph.

Figure 6 shows averaged  $p-v$  diagrams parallel to the major axis with various offsets. These  $p-v$  diagrams are obtained by averaging every  $2''$  in the range between the position offsets  $+12''$  and  $-12''$  from the major axis (see Figure 4 for this range). The red solid curve, lines, and ellipse are the same as those in Figure 5. We found that the structure of the molecular disk is not symmetric in the north-south direction. The inner disk can only be clearly seen in the position at the range between the offset  $+1''$  and  $-1''$ . The velocity feature of the bar structure can be seen in the position at the range between the offset  $+7''$  and  $-5''$ . In addition to these velocity features, we also found a rigid-rotation feature in the position at the range between the offsets  $-7''$  and  $-9''$ . The emission is weak while the slope is shallow, and the features extend

to  $\pm 40''$ , so that this structure may be a rotating disk which is located at a large radius. Here we call it an outer molecular disk.

In order to see the velocity feature of the extended structure  $OF$  in the north of the galactic disk, we averaged the  $p-v$  diagrams along the minor axis in the range between the position offsets  $+1''$  and  $-11''$  on the major axis (see Figure 4 for this range), and the averaged  $p-v$  diagram is shown in Figure 7. The strong emission is distributed along the position offset of  $\sim 0''$ , indicating the location of the galactic disk. Northern part of the galactic disk (positive side of the position offset) obviously shows an extended diffuse emission, which corresponds to the extended structure  $OF$  in Figure 3a and Figure 4. The velocity range of this diffuse emission is between  $\sim -110 - +70 \text{ km s}^{-1}$ . On the other hand, southern part of the disk (negative side of the position offset) shows no extended emission.

### 3.1.3. Mass

The total molecular gas mass can be estimated from the CO flux. The total CO flux,  $S_{\text{CO}(1-0)}$ , measured from our moment zero intensity map (Figure 3a) is  $\sim 8.01 \times 10^3 \text{ Jy km s}^{-1}$  ( $1.12 \times 10^5 \text{ K km s}^{-1} \text{ pc}^2$  from the central  $\approx 80'' \times 20''$  of the galaxy). The total flux is four times larger than that measured by Irwin & Sofue (1996) ( $\sim 2.05 \times 10^3 \text{ Jy km s}^{-1}$ ) from the same region of the galaxy. This is because our high sensitivity NMA observation provides a better sensitivity than Irwin & Sofue (1996) (as mentioned in Sec. 3.1.1) so that we can detect much weaker emission. The total molecular gas mass derived from our CO data, in units of  $M_\odot$ , can be calculated as

$$M_{\text{H}_2} = 1.2 \times 10^4 \times D^2 \times S_{\text{CO}(1-0)} \times \frac{X_{\text{CO}}}{3.0 \times 10^{20}}, \quad (1)$$

$$M_{\text{gas}} = 1.36 \times M_{\text{H}_2}, \quad (2)$$

where  $D$  is the distance in units of Mpc,  $X_{\text{CO}}$  is the CO-to- $\text{H}_2$  conversion factor in units of  $\text{cm}^{-2} \text{ K (km s}^{-1})^{-1}$ , and the factor 1.36 is a coefficient convert from molecular hydrogen gas mass to total gas mass, including helium (Sakamoto et al. 1995). Here, we used the value of  $X_{\text{CO}} = 1.4 \times 10^{20} \text{ cm}^{-2} \text{ K km s}^{-1}$  (Matsushita et al. 2000), assuming the condition of the molecular gas is similar to that of M82. Thus the total gas mass,  $M_{\text{gas}}$ , is  $\sim 1.8 \times 10^9 M_\odot$ .

The dynamical mass,  $M_{\text{dyn}}$  within the radius of  $r$ , can be derived from the rotational curve. Figure 5 shows that the maximum rotational velocity,  $v_{\text{rot}} \sim 220 \text{ km s}^{-1}$ , appears at the location of radius  $\sim 40''$  (1.5 kpc). We assume a circular rotation for the galactic disk,  $v_{\text{rot}}^2 = GM_{\text{dyn}}/r$ . Therefore, the dynamical mass within 1.5 kpc radius can be estimated as  $\sim 2 \times 10^{10} M_\odot$ . This indicates that the gas mass to dynamical mass ratio of 10%, which is the typical value for the central regions of galaxies (c.f., from 4% for Sa galaxies to 25% for Scd galaxies; Young & Scoville 1991).

## 3.2. CXO X-ray Archive Data

### 3.2.1. Image of the Diffuse Emission



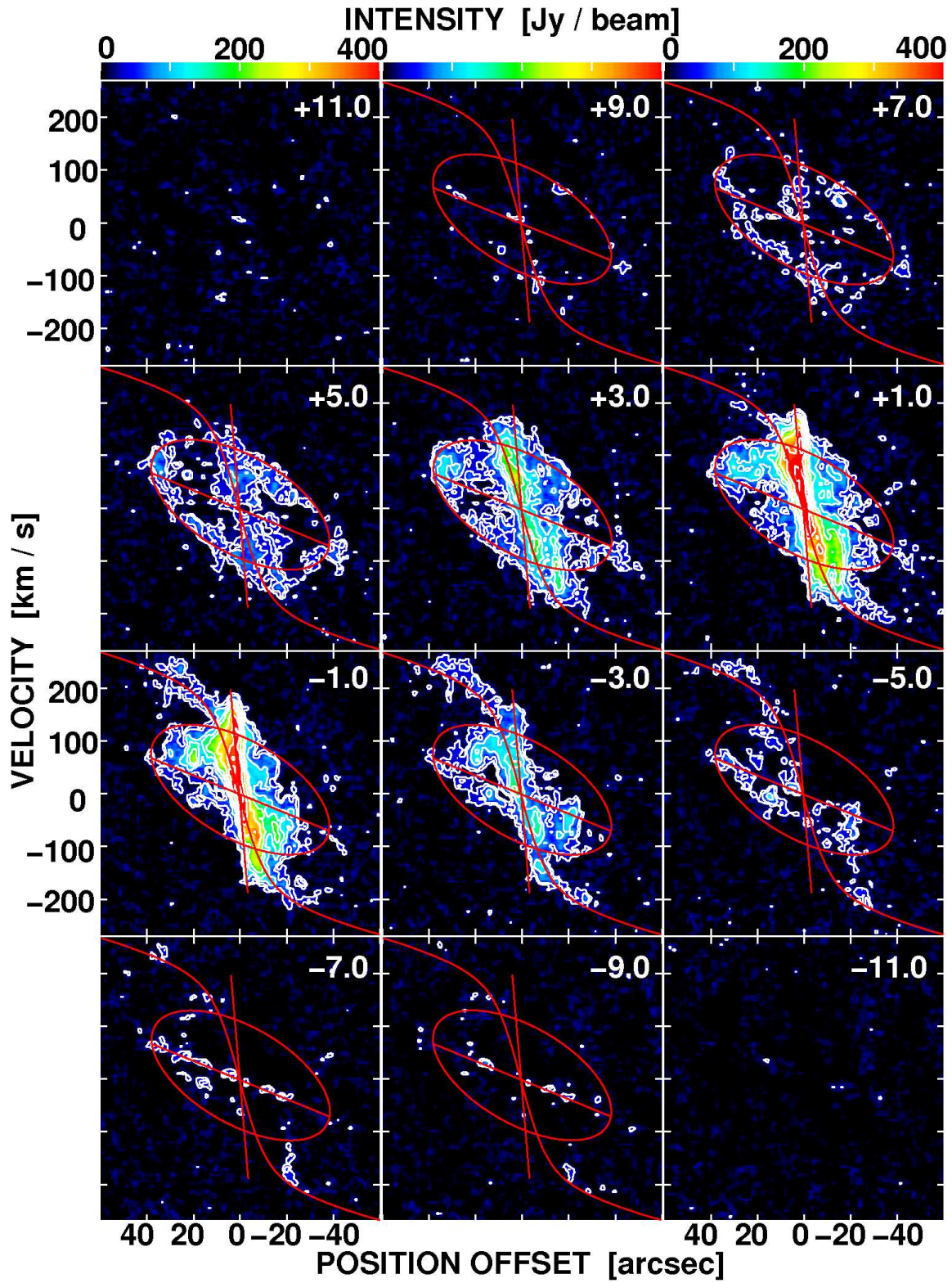


**Figure 6.** Averaged  $p-v$  diagrams parallel to the major axis in the range between the position offset of  $-12''$  and  $+12''$ , which are marked as two dashed horizontal lines in figure 4. Each  $p-v$  diagram is averaged every  $2''$  with an interval of  $2''$ . The number in each  $p-v$  diagram indicates the offset from major-axis in unit of arcsec. The solid lines, curves, and ellipses are the same as those shown in Figure 5. The zero velocity corresponds to the systemic velocity of  $840 \text{ km s}^{-1}$ . The contour levels are 3, 5, 7, 10, 20, 30, 40, and  $50\sigma$ , where  $1\sigma$  is  $9.09 \text{ mJy beam}^{-1}$ .

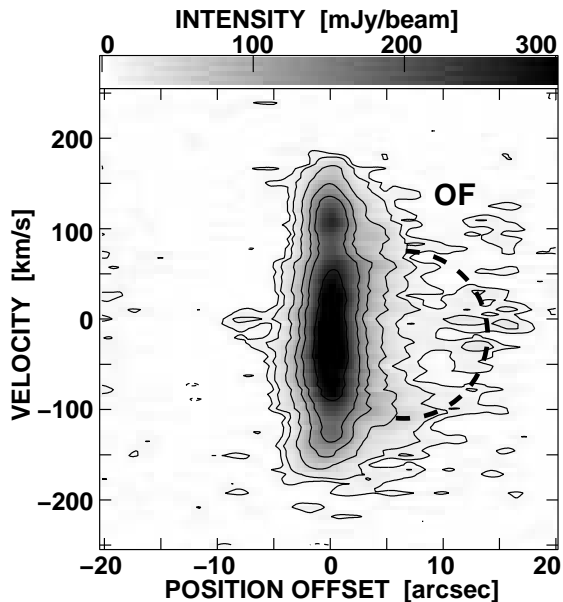


**Figure 7.** The  $p-v$  diagram along the minor axis averaged over the range between the position offsets  $+1''$  and  $-11''$  from the minor axis, which is between two dotted vertical lines in figure 4. The zero velocity corresponds to the systemic velocity of  $840 \text{ km s}^{-1}$ . The contour levels are 2, 4, 10, 20, 30, 50, and  $70\sigma$ , where  $1\sigma$  is  $5.23 \text{ mJy beam}^{-1}$ .

In order to compare the CXO X-ray data with the NMA CO(1-0) data in different scale, we made two types of smoothed images.

To image the large scale diffuse structure, we used the CIAO tool ACONVOLVE to convolve the point-source-removed X-ray image with a Gaussian that is smoothed by  $25''$  in 2 energy bands, soft ( $0.3 - 2.0 \text{ keV}$ ) and hard ( $2.0 - 7.0 \text{ keV}$ ) bands. We also tried to smooth with  $20''$ , but the diffuse emission cannot be displayed clearly. The smoothed soft and hard X-ray images are shown in Figure 8a and Figure 8b, respectively. These two images are very similar to those published by Strickland et al. (2001), suggesting that our imaging is consistent with theirs. In soft-band X-ray emission (Figure 8a), the strongest intensity is very close to the galactic center, but shifted a little bit toward the north. An asymmetric plasma outflow located above and below the galactic center is clearly seen. The northern plasma outflow has a stronger intensity and wider distribution than the southern outflow, while the southern outflow extends longer distance than the northern one. The diffuse emission spreads over  $\sim 7 - 10 \text{ kpc}$  scale in both north and south of the galactic disk. In hard-band X-ray emission (in Figure 8b), the strongest intensity is at the galactic center. The emission is roughly concentrated in the galactic center, and we do not see clear evidence of the outflow feature. The overlaid images between the CXO X-ray data and the NMA CO(1-0) data are shown in Figure 9a and Figure 9b.

To image the small scale diffuse structure, we used AIPS task CONVL to convolve the X-ray data to the same beam size as ( $3''.01 \times 2''.36$ ) as the NMA CO(1-0) data in 2 energy bands. The high resolution soft and hard X-ray images are shown in Figure 9c and Figure 9d, respectively. In the higher resolution soft-band X-ray emission map (Figure 9c), the distribution of the plasma outflow near the galactic center is roughly located in similar

region as the extended molecular gas feature *OF*, while the peak intensity of the X-ray emission is located a little bit toward the north. In the higher resolution hard-band X-ray emission map (Figure 9d), the distribution is concentrated in the galactic center.

### 3.2.2. Spectral Analysis of the Diffuse Emission

In order to compare the physical properties of plasma gas to that of molecular gas, we used XSPEC to fit the spectra of the X-ray data to obtain the temperature  $kT$ , and the normalization term  $Norm$ , which can be used to estimate mean electron density, plasma mass, thermal pressure, and thermal energy (the details will be described in Sec. 3.2.3).

For this spectral analysis, we first define spectral fitting regions. Figure 10a and Figure 10b show the VLA FIRST HI archive image (Becker et al. 1995) overlaid on the soft and hard X-ray image, respectively. The HI line emission is distributed along the galactic disk. After comparing the distribution of X-ray emission, HI emission, and the extended molecular gas *OF*, we specified/defined two fitting regions, *CORE* and *HALO*. For simplicity, we defined the region *CORE* as a circular area with a radius of  $\sim 0.3$  ( $0.67 \text{ kpc}$ ), which includes the central strong X-ray emission in the HI disk and the feature *OF* (Figure 9a, 9c, and 10a). Meanwhile, we defined the region *HALO* as a circular area with a radius of  $\sim 3.0$  ( $6.72 \text{ kpc}$ ), which includes all diffuse X-ray emission but excludes the region *CORE*.

The temperature  $kT$ , and the normalization term  $Norm$ , depend on the absorption column density and the metal abundance of the galaxy. The absorption column density of atomic hydrogen,  $N_H$ , can be fitted with the photoelectric absorption model, WABS. In *CORE*, the absorption is affected by both the host galaxy and the Milky Way. Since the absorption in the host galaxy is unknown, we left  $N_H$  as a free parameter. In *HALO*, X-ray emission has no counterpart in the HI disk, thus we only consider the absorption from the Milky Way. We therefore fixed  $N_H$  as Milky Way absorption column density,  $0.02 \times 10^{22} \text{ cm}^{-2}$  (Kalberla et al. 2005; Dickey & Lockman 1990).

For the metal abundance, we identify O ( $\sim 0.5 - 0.7 \text{ keV}$ ), Si ( $\sim 1.8 - 1.9 \text{ keV}$ ), and Fe ( $\sim 0.7 - 1.0 \text{ keV}$ ) in the *HALO* spectrum (Figure 11a), and Mg ( $\sim 1.3 - 1.4 \text{ keV}$ ), Si ( $\sim 1.8 - 1.9 \text{ keV}$ ), and Fe ( $\sim 0.7 - 1.0 \text{ keV}$ ) in the *CORE* spectrum (Figure 11b). The existence of these lines suggests that the emission originates from optically-thin thermal plasma (Inui et al. 2005). Thus we can choose a thermal-plasma model from XSPEC, i.e., VMEKAL or VAPEC.

Since the data quality of the *HALO* spectrum is poor at energy lower than  $0.4 \text{ keV}$  and higher than  $1.3 \text{ keV}$ , we intended to exclude these data. In addition to considering the metal abundance of Si at  $\sim 1.8 - 1.9 \text{ keV}$ , we include data at higher energy side till  $3.0 \text{ keV}$ . Therefore, the soft-band energy range is  $0.4 - 3.0 \text{ keV}$ . We begin to fit the spectrum with an absorbed single-temperature thermal-plasma model. However, the spectrum cannot be fitted well neither by WABS\*VMEKAL nor by WABS\*VAPEC model. Thus we tried to fit the spectrum via an absorbed two-temperature thermal-plasma model, i.e., WABS\*(VMEKAL + VMEKAL) or WABS\*(VAPEC + VAPEC). We also fix the metal abun-



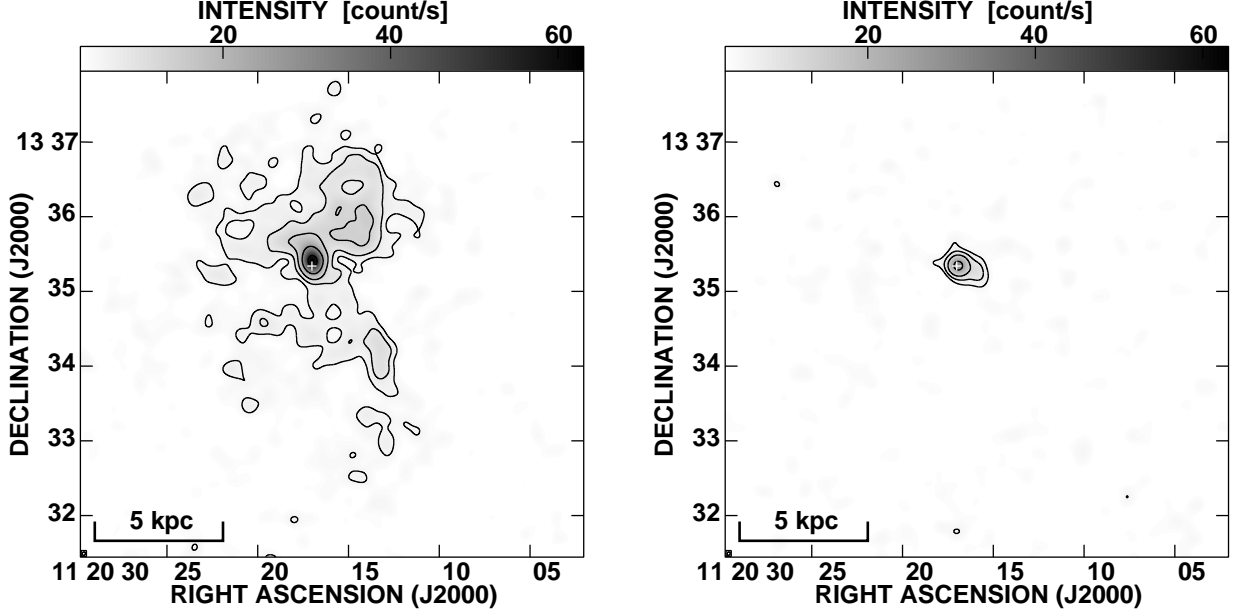


**Figure 8.** Smoothed (by  $25''$ ) CXO X-ray image after removing point sources. The cross is the phase tracking center of the NMA CO(1-0) data at  $\alpha(\text{J2000}) = 11^{\text{h}}20^{\text{m}}04^{\text{s}}.863$  and  $\delta(\text{J2000}) = 13^{\circ}30'50''.49$ . (a) Soft band (0.3 – 2.0 keV). The contour levels are 2, 3, 5, 10, and  $20 \times 2.6757 \text{ counts s}^{-1}$ . (b) Hard band (2.0 – 7.0 keV). The contour levels are 2, 3, 5, and  $10 \times 2.5802 \text{ counts s}^{-1}$ .

dances of the higher temperature component to those of the lower temperature component. The fitting results show that the model WABS\*(VMEKAL + VMEKAL) fits better than the model WABS\*(VAPEC + VAPEC). The fitting parameters in the model WABS\*(VMEKAL + VMEKAL) for both *HALO* and *CORE* regions are listed in Table 1.

In *HALO*, the metal abundances fitted by the model are  $\sim 0.5 Z_{\odot}$  for O,  $\sim 2.8 Z_{\odot}$  for Si, and  $\sim 0.4 Z_{\odot}$  for Fe, where  $Z_{\odot}$  is the solar abundance. Two temperatures are  $\sim 0.21 \text{ keV}$  and  $0.60 \text{ keV}$ . In *CORE*, the metal abundances fitted by the model are  $\sim 5.0 Z_{\odot}$  for Mg,  $\sim 13.5 Z_{\odot}$  for Si, and  $\sim 0.8 Z_{\odot}$  for Fe. Two temperatures are  $\sim 0.47 \text{ keV}$  and  $7.3 \text{ keV}$ . We notice that both the metal abundance of Mg and Si are extremely high. These values are likely not physical. Besides, their large uncertainties ( $1.5 - 25.9 Z_{\odot}$  for Mg and  $5.3 - 50.8 Z_{\odot}$  for Si) suggest that the fitted values are not accurate enough. One possible reason is that the CCD material contaminates the detection of Si. Another possible reason is that the photon counts,  $\sim 1000$  counts, are too low to get a reasonable fitting results for Mg and Si. We fix the metal abundances of Mg and Si as unity and re-fit the spectrum again. This does not change  $kT$  and  $Norm$  too much. Therefore, we could ignore the influence from high abundances of Mg and Si.

### 3.2.3. The Properties of Plasma Gas

From  $kT$  and  $Norm$ , we could derive mean electron density  $n_e$ , plasma mass  $M_{\text{plm}}$ , thermal pressure  $P_{\text{plm,thm}}$ , and thermal energy  $E_{\text{plm,thm}}$ . The definition of  $Norm$  is <sup>1</sup>

$$Norm = \frac{10^{-14}}{4\pi(D_A(1+z))^2} EI, \quad (3)$$

<sup>1</sup> The definition is from XSPEC website, <http://heasarc.gsfc.nasa.gov/docs/xanadu/xspec/manual/>

where  $EI$  is the emission integral,

$$EI = \int n_e n_H f dV, \quad (4)$$

$D_A$  is angular diameter distance,  $z$  is redshift,  $V$  is the volume of plasma,  $n_H$  is the hydrogen density, and  $f$  is the volume filling factor. For nearby galaxies,  $D_A$  is simply the distance  $D$ . Assuming that the electron and hydrogen have the same density, i.e.,  $EI = \int n_e^2 f dV$ , we can derive the following plasma properties.

The mean electron number density of plasma is,

$$n_e = \left( \frac{EI}{Vf} \right)^{1/2}. \quad (5)$$

The mass of plasma is,

$$M_{\text{plm}} = \rho_{\text{plm}} V = m_p n_e V, \quad (6)$$

where  $\rho_{\text{plm}}$  is the mass density of plasma, and  $m_p$  is the proton mass. The thermal pressure of plasma is,

$$P_{\text{plm,thm}} = \frac{\rho_{\text{plm}}}{\mu m_p} kT = 2n_e kT, \quad (7)$$

where  $\mu$  is the mean molecular weight. For a fully ionized hydrogen, there are two particles for every proton and  $\mu = 1/2$ . The thermal energy of plasma is,

$$E_{\text{plm,thm}} = \frac{3}{2} P_{\text{plm,thm}} V = 3n_e V kT \quad (8)$$

(Carroll & Ostlie 1996).

We applied  $z = 0.0028$  base on the systemic velocity measured from our NMA CO(1-0) data. The derived plasma parameters from the two-temperature model in *HALO* and *CORE* regions are shown in Table 2.

The electron densities of the lower and the higher temperature component in *CORE* are  $9.5 f^{-1/2} \times 10^{-3} \text{ cm}^{-3}$  and  $2.0 f^{-1/2} \times 10^{-2} \text{ cm}^{-3}$ , respectively, about one order of magnitude higher than those in *HALO*. The plasma

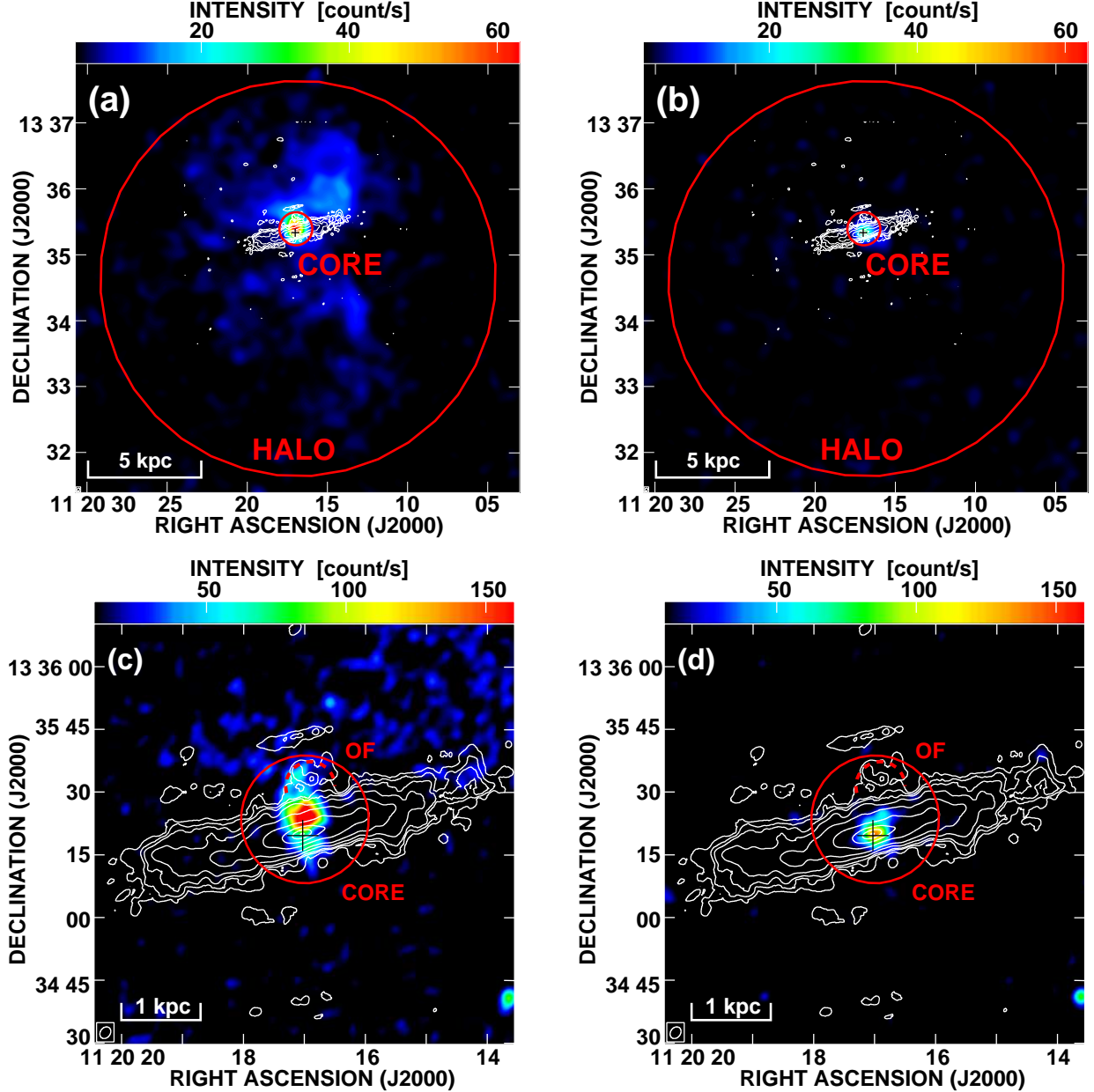


**Figure 9.** The spatial correlation between the NMA CO(1-0) data (contours) and the CXO X-ray data (color scale). The contour levels are the same as those in Figure 3. The cross is the phase tracking center of the NMA CO(1-0) data. The large and small red solid circles are the regions *HALO* and *CORE*, respectively. The red dashed curve is the *OF*. (a) CO(1-0) contours overlaid on the soft band (0.3 – 2.0 keV) X-ray image. (b) CO(1-0) contours overlaid on the hard band (2.0 – 7.0 keV) X-ray image. (c) Zoom-in image of the central  $2' \times 2'$  region of (a). (d) Zoom-in image of the central  $2' \times 2'$  region of (b).

masses of the lower and the higher temperature component in *CORE* are  $3.0f^{1/2} \times 10^5 M_\odot$  and  $6.4f^{1/2} \times 10^5 M_\odot$ , respectively, about one to two orders of magnitude smaller than those in *HALO*. The plasma thermal pressures of the lower and the higher temperature component in *CORE* are  $1.4f^{-1/2} \times 10^{-11} \text{ dyne cm}^{-2}$  and  $4.8f^{-1/2} \times 10^{-10} \text{ dyne cm}^{-2}$ , respectively, about one to two orders of magnitude higher than those in *HALO*. The plasma thermal energies of the lower and the higher temperature component in *CORE* are  $0.8f^{1/2} \times 10^{54} \text{ erg}$  and  $2.7f^{1/2} \times 10^{55} \text{ erg}$ , respectively, about one order of magnitude smaller than those in *HALO*.

### 3.3. The Extended Structure above Galactic Disk

Our NMA CO(1-0) observations detected an extended structure *OF* that appears only in the north of the galactic disk for the first time (Figure 3a). After comparing the morphology between the NMA CO(1-0) data and the CXO X-ray data (Figure 8a, Figure 9c, and Figure 9d), we found that the distribution of *OF* is roughly matching the northern plasma outflow near the galactic center (*CORE*), and seems to be the ejection point of the northern large-scale plasma outflow. The intensity peak of X-ray emission is a little bit toward the north of *OF*, which is similar to NGC 2146 (Tsai et al. 2009). Combining the kinematic feature of *OF* in the  $p-v$  diagram (Figure 7), we conclude that *OF* is a molecular outflow and is part of the large-scale *HALO* outflow.

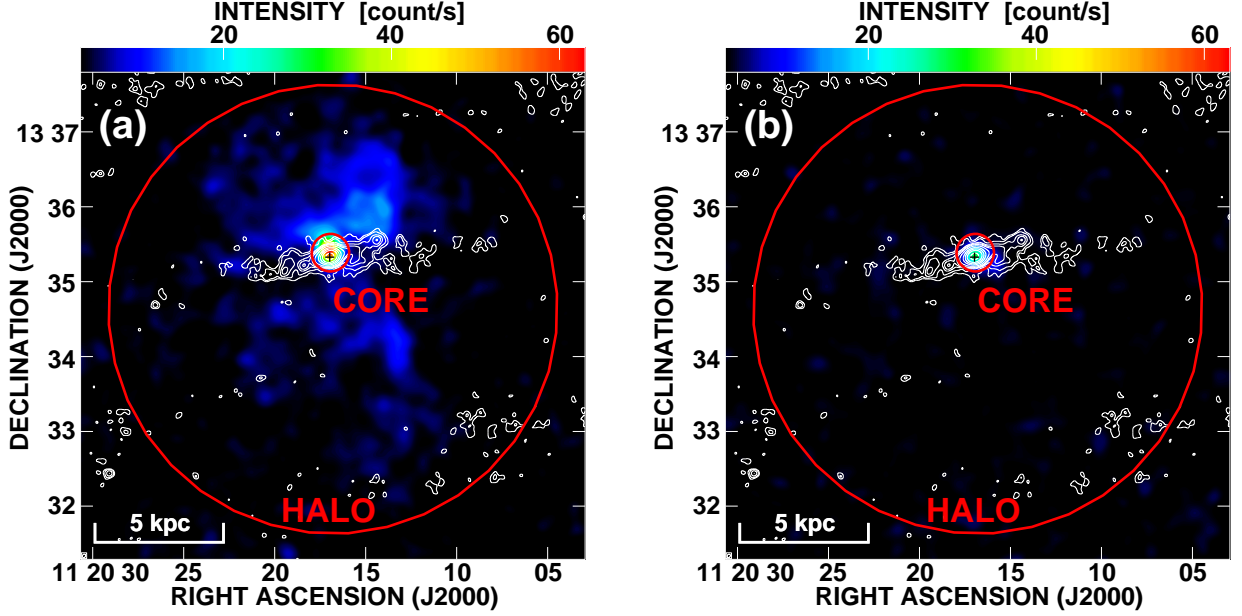


**Figure 10.** Smoothed (by  $25''$ ) CXO X-ray image (color) overlaid on the HI VLA FIRST data (contour). The cross is the phase tracking center of the NMA CO(1-0) data. (a) HI contours overlaid on the soft-band (0.3 – 2.0 keV) X-ray image. (b) HI contours overlaid on the hard-band (2.0 – 7.0 keV) X-ray image. The contour levels are 2, 3, 5, 7, 10, 20, 50, 100, 200, and 500 $\sigma$ , where  $1\sigma$  is 0.15 mJy beam $^{-1}$ .

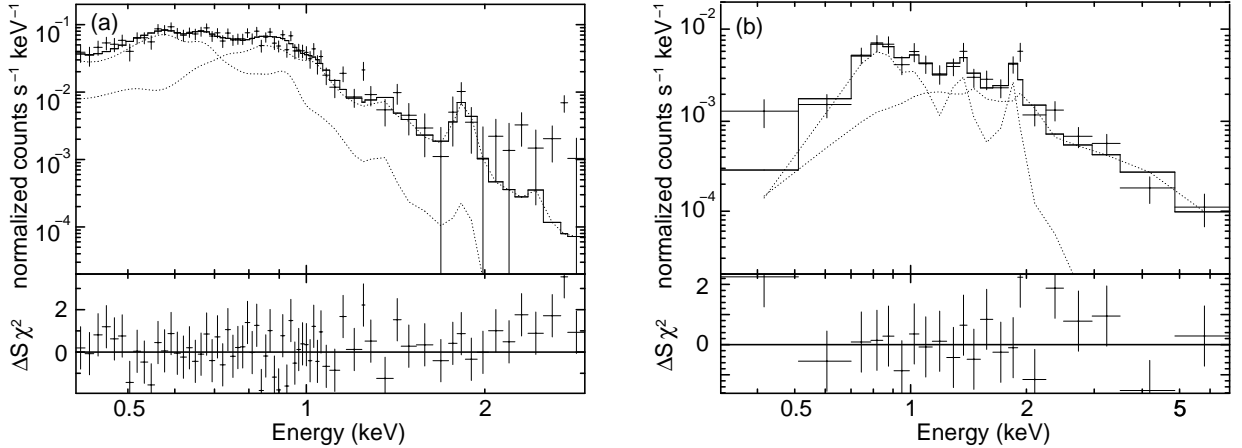


**Figure 11.** The CXO X-ray data with the fitted XSPEC model. The top plots in each figure are the data (crosses) with the fitted model (dot for individual model and histogram for combined model). The bottom plots in each figure are  $\chi^2$ . (a) Spectrum extracted from the *HALO* region with the fitting model of WABS\*(VMEKAL + VMEKAL). (b) Spectrum extracted from the *CORE* region with the fitting model of WABS\*(VMEKAL + VMEKAL). The fitting parameters are shown in Table 1.

The expansion velocity and the size of *OF* can be estimated from the averaged minor-axis  $p-v$  diagram. In Figure 7, the velocity range of *OF* is about  $\sim 180$  km s $^{-1}$  (Sec. 3.1.2). Since we do not see clear velocity gradient in a certain direction, the simplest model for *OF* is an expanding outflow that explodes isotropically at one side of the disk (see the dashed curve in Figure 7). The expansion velocity and radius, which measured from the  $p-v$  diagram, are  $v_{\text{exp}} \sim 90 \pm 10$  km s $^{-1}$  and  $R_{\text{of}} \sim 10'' - 12'' \sim 370 - 450$  pc, respectively.

The molecular mass of *OF* can be estimated from CO flux. The total flux, summed from each channel map, is 82.0 Jy km s $^{-1}$  ( $= 1.14 \times 10^3$  K km s $^{-1}$ ). Using Eq. 1 and Eq. 2, assuming the same conversion factor, we can derive the gas mass of *OF*,  $M_{\text{of}}$ , as  $2.8 \times 10^7 M_{\odot}$ . The mass is only a few percent of the total molecular gas detected in our data.

The mechanical energy is  $E_{\text{of,mech}} = \frac{1}{2} M_{\text{of}} v_{\text{exp}}^2 = (1.8 - 2.8) \times 10^{54}$  erg. After considering the mechanical efficiency  $\gamma$ ,  $\sim 10 - 20$  %, the energy transmitting from supernova explosions into the surrounding ISM (McCray & Kafatos 1987; Weaver et al. 1977; Larson 1974). The energy corresponds to 9,000 – 28,000 supernova explosions. Assuming the expansion velocity keeps constant, the expansion timescale is  $t_{\text{exp}} = R_{\text{of}}/v_{\text{exp}} = 3.3 - 6.8$  Myr. The average molecular gas mass flow rate can be calculated after taking account the expansion timescale,  $\dot{M}_{\text{of}} = M_{\text{of}}/t_{\text{exp}} \sim 4.1 - 8.5 M_{\odot} \text{ yr}^{-1}$ .

#### 4. DISCUSSION

##### 4.1. Bar, Disk, or Superbubbles?

Irwin & Sofue (1996) claimed that they detected four molecular superbubbles mostly associated with the low velocity gradient ridge outside of the nuclear disk. The

locations and the expansion velocities of these four molecular superbubbles are shown in Figure 9 and Table 2 of Irwin & Sofue (1996). Two superbubbles, A and C in Irwin & Sofue (1996), are located at the same position and have the same central velocity but different expansion velocities. Another two superbubbles, B and D in Irwin & Sofue (1996), are located at different positions and have different central velocities.

In order to confirm these four structures are real superbubbles from our data, we used two types of images, the  $p-v$  diagrams (Figure 12) and the intensity maps (Figure 13), to examine these structures. We parametrized these structures with four parameters,  $(\Delta\alpha, \Delta\delta, v_c, v_{\text{exp}})$ , where  $\Delta\alpha$  and  $\Delta\delta$  specify the location,  $v_c$  is the central velocity of the superbubble, and  $v_{\text{exp}}$  is the expansion velocity of the superbubble. The big blue dot in each  $p-v$  diagram of Figure 12 is to mark the position and the central velocity of each superbubble. The cross in each integrated intensity map of Figure 13, which is integrated along superbubble's expansion velocity, is to mark the central location of the superbubble.

Superbubble A has a coordinate of  $(-13'', 0'', 55 \text{ km s}^{-1}, 20 \text{ km s}^{-1})$ . In the  $p-v$  diagram of Figure 12a, we do not find any expanding structure at position A. In addition, in the intensity map of Figure 13a, which is integrated along the velocity range of  $35 - 75 \text{ km s}^{-1}$ , we do not see any extended/distorted structure at position A. Since it is difficult to match superbubble A at position A both in the  $p-v$  diagram and the intensity map, it is difficult to conclude structure A as a superbubble. Meanwhile, the position A in Figure 12a is close to the red ellipse, which represents the  $p-v$  diagram of a bar structure. This suggests that structure A is more likely part of the bar rather than a superbubble.

Superbubble B has a coordinate of  $(-33'', -1'', -62 \text{ km s}^{-1}, 33 \text{ km s}^{-1})$ . Its  $p-v$  diagram is shown in Figure 12b, and its intensity map, which is integrated along the velocity range of  $29 - 95 \text{ km s}^{-1}$ , is shown in Figure 13b. Unfortunately, we do not find any expanding structure at position B in the  $p-v$  diagram (Figure 12b), neither find any shell structure at the position B in the intensity map (Figure 13b). Thus it is also difficult to identify structure B as a superbubble. Besides, since position B in the  $p-v$  diagram is located inside the red ellipse, it is also possible to consider structure B as part of the bar. On the other hand, the emission distribution at position B in the  $p-v$  diagram looks different from that at its symmetric position, which has a coordinate of  $(33'', -1'', 62 \text{ km s}^{-1}, 33 \text{ km s}^{-1})$ . Namely, there is almost no emission at position B, but there is emission detected at its symmetric position. An explanation for this asymmetric is that the molecular gas at the position B has been blown up. This indicates a possibility of the existence of a superbubble at position B in the past. However, we can not distinguish which scenario is true. Therefore, it is also difficult to conclude that structure B is a superbubble.

Superbubble C has a coordinate of  $(-13'', 0'', 55 \text{ km s}^{-1}, 150 \text{ km s}^{-1})$ , which has very similar coordinate with that of superbubble A. The only difference is their expansion velocities. Thus we can examine superbubble C by using the same  $p-v$  diagram with that

of superbubble A (Figure 12a). Again, we cannot find any emission represents superbubble C. Thus it is still difficult to identify structure C as a superbubble.

Superbubble D has a coordinate of  $(-20'', -5'', -126 \text{ km s}^{-1}, 85 \text{ km s}^{-1})$ . We find emission detected at position D in the  $p-v$  diagram of Figure 12c. In addition, in the intensity map of Figure 13c, which is integrated the velocity range between  $-211$  and  $-41 \text{ km s}^{-1}$ , we find an extended structure at the position D. We further check the  $p-v$  diagram (Figure 14) averaged between position offsets  $-16''$  and  $-24''$  along the minor axis of Irwin & Sofue's major axis (i.e., clockwise rotation of  $17^\circ$ ) in order to compare the two observations. We depict their superbubble D in Figure 14 by a thin cross and a thin dashed ellipse. Interestingly, our deep observation detected more diffuse emission. The enclosed loop marked as a thick dashed ellipse, which represents the structure of a superbubble, is smaller than that of Irwin & Sofue's thin dashed loop. We identify the thick loop as the superbubble D' with a coordinate of  $(-20'', -4'', -138 \text{ km s}^{-1}, 50 \text{ km s}^{-1})$ . Since a shift of  $1''$  from superbubble D is smaller than the angular resolution of  $\sim 3''$ , we conclude that the superbubble D and D' are identical, but the superbubble D' has a more accurate coordinate than the superbubble D. The radius of the superbubble D' can be estimated from Figure 12c and Figure 14,  $\sim 5'' \times 5''$  ( $\sim 186 \text{ pc} \times 186 \text{ pc}$ ).

In conclusion, our results only confirm the existence of the superbubble D, superbubble A and C are likely to be parts of the bar structure, while superbubble B could be either part of the bar structure, or a past superbubble whose molecular gas has already been blown up. The mis-interpretation is possibly due to the low sensitivity of the previous observation.

#### 4.2. The Molecular Outflow is still Moving Outward?

In order to figure out the evolution of the molecular outflow *OF*, we compare the pressure between the diffuse molecular gas *OF* and the plasma gas in the *CORE* region.

In the molecular outflow *OF*, the thermal pressure of constituent molecular cloud can be derived by  $P_{\text{of,thm}} = n_{\text{of}}kT$ , where  $n_{\text{of}}$  is the number density of *OF*. Since we do not have density and temperature information of *OF*, we simply adopt typical values ( $100 - 1000 \text{ cm}^{-3}$  and  $10 - 100 \text{ K}$ ) for CO(1-0) emitting gas. Thus the thermal pressure of *OF* is  $1.4 \times 10^{-(11-13)} \text{ dyne cm}^{-2}$ .

In *CORE* region, the thermal pressures of the plasma outflow in the lower and the higher temperatures are  $1.4f^{-1/2} \times 10^{-11} \text{ dyne cm}^{-2}$  and  $4.8f^{-1/2} \times 10^{-10} \text{ dyne cm}^{-2}$ , respectively (see Sec. 3.2.3 and Tab. 2). Adopting a volume filling factor of  $0.1 - 0.01$ , their thermal pressures are  $(0.5 - 1.4) \times 10^{-10} \text{ dyne cm}^{-2}$  and  $(1.5 - 4.8) \times 10^{-9} \text{ dyne cm}^{-2}$ , respectively. Besides, the ram pressure that *OF* suffered from the plasma outflow can be derived by  $P_{\text{ram}} = \rho_{\text{plm}} \times v_{\text{rel}}^2$ , where  $v_{\text{rel}} = |v_{\text{exp}} - v_{\text{plm}}|$  is the relative velocity between the expansion velocity of *OF*,  $v_{\text{exp}}$ , and of the plasma outflow,  $v_{\text{plm}}$ . We assume that the expansion velocity of the plasma outflow is similar to its thermal velocity, i.e.,  $v_{\text{plm}} \sim \sqrt{3kT/\mu m_p}$ . Thus  $v_{\text{plm}}$  estimated from the lower and the higher temperature components in the *CORE* are  $520$  and  $2,050 \text{ km s}^{-1}$ , respectively. Since  $v_{\text{exp}} \sim 90 \text{ km s}^{-1}$ ,  $v_{\text{rel}}$  for the lower

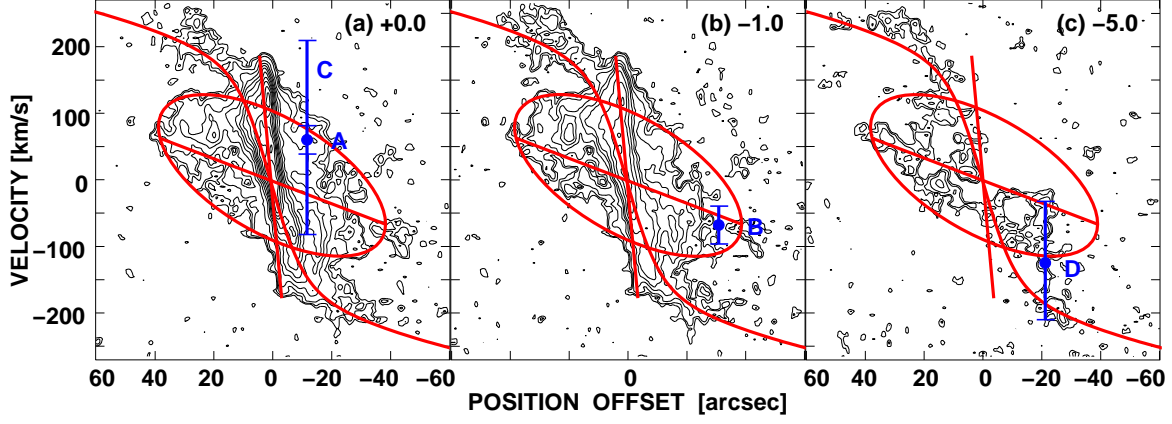


**Figure 12.** Our NMA CO(1-0)  $p-v$  diagrams marked with the position of superbubbles claimed by Irwin & Sofue (1996). The red curve, solid lines, and ellipse are the same with those in Figure 5. The big blue dot in each  $p-v$  diagram indicates the central velocity ( $v_c$ ) of the superbubble claimed by Irwin & Sofue (1996). The blue bar indicates the expansion velocity ( $v_{\text{exp}}$ ) of superbubbles. The contour levels are 2, 3, 5, 10, 15, 20, ..., and  $50\sigma$ , where  $1\sigma = 9.09 \text{ mJy beam}^{-1}$ . (a) The major-axis  $p-v$  diagram. Two superbubble A and C have the same central velocity of  $55 \text{ km s}^{-1}$ . Their expansion velocities are  $20 \text{ km s}^{-1}$  and  $150 \text{ km s}^{-1}$ , respectively. (b) The  $p-v$  diagram parallel to the major axis with offset of  $-1.0''$ . The superbubble B has a central velocity of  $-62 \text{ km s}^{-1}$  and an expansion velocity of  $33 \text{ km s}^{-1}$ . (c) The  $p-v$  diagram parallel to the major axis with offset of  $-5.0''$ . The superbubble D has a central velocity of  $-126 \text{ km s}^{-1}$  and an expansion velocity of  $85 \text{ km s}^{-1}$ .

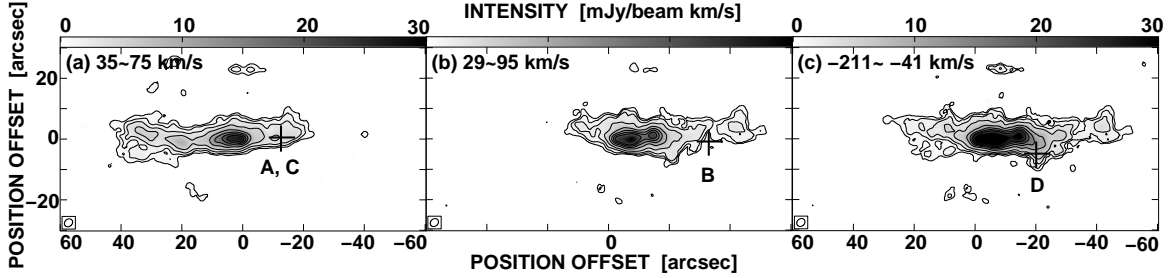


**Figure 13.** The integrated intensity maps. The crosses mark the positions of superbubbles A, B, C, and D. (a) Integrated velocity range between 35 and  $75 \text{ km s}^{-1}$ . The contour levels are 2, 5, 10, 20, 40, 60, 80, 100, 150, and  $200\sigma$ , where  $1\sigma = 219.45 \text{ mJy beam}^{-1} \text{ km s}^{-1}$ . (b) Integrated velocity range between 29 and  $95 \text{ km s}^{-1}$ . The contour levels are 2, 5, 10, 20, 40, 60, 80, 100, and  $150\sigma$ , where  $1\sigma = 194.75 \text{ mJy beam}^{-1} \text{ km s}^{-1}$ . (c) Integrated velocity range between  $-211$  and  $-41 \text{ km s}^{-1}$ . The contour levels are 2, 5, 10, 20, 40, 60, 80, and  $100\sigma$ , where  $1\sigma = 229.70 \text{ mJy beam}^{-1} \text{ km s}^{-1}$ .

and the higher temperature components in the *CORE* are  $430$  and  $1,960 \text{ km s}^{-1}$ , respectively, then the ram pressures of the lower and the higher temperature components are  $2.9 f^{-1/2} \times 10^{-11} \text{ dyne cm}^{-2}$  and  $1.3 f^{-1/2} \times 10^{-9} \text{ dyne cm}^{-2}$ , respectively. After considering a filling factor of  $0.01 - 0.1$ , the ram pressures are  $(0.9 - 3.1) \times 10^{-10} \text{ dyne cm}^{-2}$  and  $(0.4 - 1.3) \times 10^{-8} \text{ dyne cm}^{-2}$ , respectively. We notice that in the lower temperature components, the ram pressure and the plasma thermal pressure have similar values, while in the higher temperature components, the ram pressure is higher than the plasma thermal pressure. Generally speaking, the ram pressures and the plasma thermal pressures in *CORE* are  $\sim 10^{-(8-10)} \text{ dyne cm}^{-2}$ . Since the thermal pressure of the molecular outflow *OF* is  $\sim 10^{-(11-13)} \text{ dyne cm}^{-2}$  (Sec. 4.2), this indicates that the *OF* is pushed by the plasma gas. Thus we conclude that the *OF* is still moving outward.

#### 4.3. The Evolutionary Stage of the Starburst Activity

In order to figure out the evolutionary stage of the starburst activity, we defined an evolutionary parameter,  $\tau$ , which is the expansion timescale of molecular outflow,

$t_{\text{exp}}$ , normalized to the total starburst timescale,  $t_{\text{SB}}$ ,

$$\tau = \frac{t_{\text{exp}}}{t_{\text{SB}}}, \quad (9)$$

$$= \frac{t_{\text{exp}}}{t_{\text{exp}} + t_{\text{cons}}}, \quad (10)$$

where  $\tau = 1$  means the starburst period is finished, and  $t_{\text{SB}}$  includes two timescales,  $t_{\text{exp}}$ , implying the timescale from the beginning of the starburst to now, and  $t_{\text{cons}}$ , the molecular gas consumption timescale, i.e., the timescale that the current molecular gas in the starburst region to be used up, implying the timescale from now to the end of starburst period.  $t_{\text{cons}}$  is highly depending on two processes, mass loss through molecular outflow, and star formation,

$$t_{\text{cons}} = \frac{M_{\text{SBR}}}{\dot{M}_{\text{of}} + \text{SFR}}, \quad (11)$$

where  $M_{\text{SBR}}$  is the molecular gas mass in the starburst region, and the SFR is the star formation rate.

From Sec. 3.3, we know the mass loss rate,  $\dot{M}_{\text{of}} = 4.1 - 8.5 M_{\odot} \text{ yr}^{-1}$ . We define the size of the starburst region as the same with the base size of the X-ray emission,



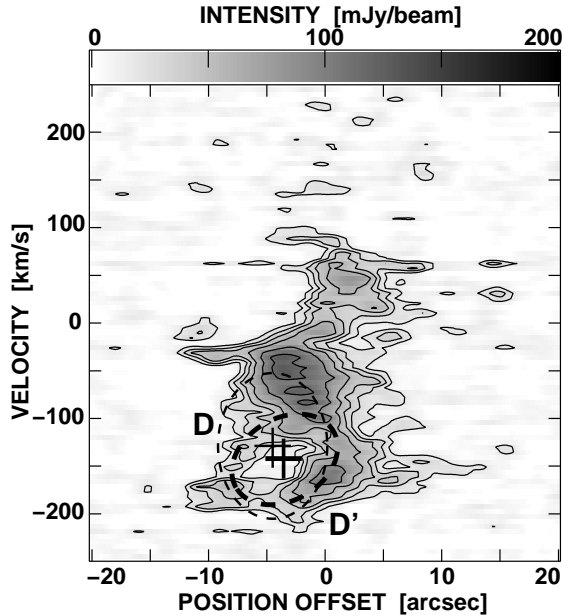


**Figure 14.** The minor-axis  $p-v$  diagram of the superbubble D. This is averaged between  $-18''$  and  $-22''$  along minor axis after rotating  $17^\circ$ , the same rotating degree with that of Irwin & Sofue (1996). The contour levels are 3, 5, 7, 10, 15, and  $20\sigma$ , where  $1\sigma = 5.78 \text{ mJy beam}^{-1}$ . The thin cross and the thin dashed circle indicate the central position/velocity and the expansion velocity, respectively, of superbubble D identified by Irwin & Sofue (1996). From our NMA data, we re-identify the superbubble as D'. The thick dashed ellipse indicates the shell structure of superbubble D'. The thick cross indicates the central position of superbubble D'.

which is  $\sim 0.5 \text{ kpc}$ . Since the CO flux within starburst region is  $\sim 450 \text{ Jy km s}^{-1}$ , this leads the molecular gas mass to be  $\sim 2.0 \times 10^8 M_\odot$ . Since our data do not provide any information of the SFR, we use IR luminosity,  $L_{\text{IR}}$ , to estimate the SFR as the upper limit. We assume that the IR luminosity is all contributed from the central starburst region, thus the SFR in the starburst region can be estimated as,  $\text{SFR} = 4.5 \times 10^{-44} L_{\text{IR}}$  (Kennicutt 1998). Taking  $L_{\text{IR}} = 10^{10.25} L_\odot$  (Sanders et al. 2003), SFR is  $3.2 M_\odot \text{ yr}^{-1}$ . Thus  $t_{\text{cons}}$  of NGC 3628 is calculated as 17 – 27 Myr.

Adopting a molecular outflow expansion timescale of 3.3 – 6.8 Myr (from Sec. 3.3), we have  $t_{\text{SB}} = 20 - 34 \text{ Myr}$ , and  $\tau = 0.11 - 0.25$ . This suggests that the evolutionary stage of the starburst activity is relatively young.

### 5. SUMMARY

Our NMA CO(1-0) observations detected a sub-kpc  $\sim 370 - 450 \text{ pc}$  scale molecular outflow for the first time with an expansion speed of  $\sim 90 \pm 10 \text{ km s}^{-1}$  in the starburst galaxy NGC 3628. The molecular outflow mass is  $2.8 \times 10^7 M_\odot$ , the expansion timescale is 3.3 – 6.8 Myr, and the mechanical energy is  $(1.8 - 2.8) \times 10^{54} \text{ erg}$ .

In order to understand the evolution of molecular outflow and the relation with the plasma outflow, we compared our NMA CO(1-0) data with the CXO X-ray archival data. We estimated the total energy both from mechanical energy of molecular outflow and thermal energy of plasma outflow. The total energy generated by the starburst activity is estimated as  $(2.3 - 2.8) \times 10^{55} \text{ erg}$ . The thermal pressure of the molecular outflow is  $\sim 10^{-(11-13)} \text{ dyne cm}^{-2}$ . The thermal pres-

sure and the ram pressure of the plasma outflow are  $\sim 10^{-(8-10)} \text{ dyne cm}^{-2}$ . This indicates that the molecular outflow is still pushed by the plasma gas and is moving outward. Besides, we confirmed one superbubble as a real structure from the four superbubbles that Irwin & Sofue (1996) claimed. Two of them should be just noise, and the other one is difficult to be concluded.

We also estimated the molecular gas consumption timescale, 17 – 27 Myr. This yields a total starburst timescale to be 20 – 34 Myr with an evolutionary parameter of 0.11 – 0.25, suggesting that the starburst activity in NGC 3628 is still in a young stage.

We appreciate to Yi-Jung Yang, I-Non Chiu, and Dr. Sandor Molnar for exchanging ideas of X-ray data analysis, and to Dr. Kazushi Sakamoto and Prof. Mousumi Das Amarnath for several suggestion on this paper. We also thank the anonymous referee for very useful comments. We are grateful to the NRO staff for the operation and improvement of the NMA. This work is supported by the National Science Council (NSC) of Taiwan, NSC 97-2112-M-001-021-MY3 and NSC 100-2112-M-001-006-MY3.

### REFERENCES

- Alatalo, K., Blitz, L., Young, L. M., et al. 2011, *ApJ*, 735, 88
- Armus, L., Heckman, T. M., & Miley, G. K. 1990, *ApJ*, 364, 471A
- Becker, R. H., White, R. L., Helfand, D. J. 1995, *ApJ*, 450, 559
- Binney, J., Gerhard, O. E., Stark, A. A., Bally, J. & Uchida, K. I. 1991, *MNRAS*, 252, 210
- Carroll, B. W., & Ostlie, D. A. 1996, *An Introduction to Modern Astrophysics* (Addison Wesley Publishing Company)
- Cecil, G., Bland-Hawthorn, J., & Veilleux, S. 2002, *ApJ*, 576, 745
- Charles, P. A., & Seward, F. D. 1995, *Exploring the X-ray Universe* (Cambridge: Cambridge University Press)
- Chevalier, R. A., & Clegg, A. W. 1985, *Nature*, 317, 44
- Chromey, F. R., Elmegreen, D. M., Mandell, A., & McDermott, J. 1998, *ApJ*, 115, 2331
- Chung, A., Yun, M. S., Naraynan, G., Heyer, M., & Erickson, N. R. 2011, *ApJ*, 732, 15
- Cole, G. H. J., Mundell, C. G., & Pedlar, A. 1998, *MNRAS*, 300, 656
- Condon, J. J., Condon, M. A., Gisler, G., & Puschell, J. J. 1982, *ApJ*, 252, 102
- Cooper, J. L., Bicknell, G. V., & Sutherland, R. S. 2008, *ApJ*, 674, 157
- Dahlem, M., Heckman, T. M., Fabbiano, G., Lehnert, M. D., & Gilmore, D. 1996, *ApJ*, 461, 724
- Dickey, J. M. & Lockman, F. J. 1990, *ARA&A*, 28, 215
- Englmaier, P. & Gerhard, O. 1999, *MNRAS*, 304, 512
- Feruglio, C., Maiolino, R., Piconcelli, E., et al. 2010, *A&A*, 518, L155
- Fisher, J., Sturm, E., González-Alfonso, E., et al. 2010, *A&A*, 518, 41
- García-Burillo, S. & Guélin, M. 1995, *A&A*, 299, 675
- Heckman T. M., Armus, L., & Miley, G. K. 1990, *ApJS*, 74, 833
- Inui, T., Matsumoto, H., Tsuru, T. G., et al. 2005, *PASJ*, 57, 135
- Irwin, J. A. & Sofue, Y. 1996, *ApJ*, 464, 738
- Kalberla, P. M. W., Burton, W. B., Hartmann, D., et al. 2005, *A&A*, 440, 775
- Kenninutt, R. C., Jr. 1998, *ARA&A*, 36, 189
- Larson, R. B. 1974, *MNRAS*, 169, 229
- Lehnert, M. D., & Heckman, T. M. 1996, *ApJ*, 462, 651
- Matsushita, S., Muller, S., & Lim, J. 2007, *A&A*, 468, L49
- Matsushita, S., Kawabe, R., Kohno, K., et al. 2005, *ApJ*, 618, 712
- Matsushita, S., Kawabe, R., Matsumoto, H., et al. 2000, *ApJ*, 545, L107
- McCray, R. & Kafatos, M. 1987, *ApJ*, 317, 190

**Table 1**  
Spectral Models for the CXO Spectra

Region	$N_H$ (1)	$kT_1$ (2)	Norm <sub>1</sub> (3)	$kT_2$ (4)	Norm <sub>2</sub> (5)	O (6)	Mg (7)	Si (8)	Fe (9)	Red. $\chi^2$ (10)	D.O.F. (11)
HALO <sup>a</sup>	0.02*	$0.21^{+0.03}_{-0.02}$	$8.52^{+0.04}_{-0.05}$	$0.60^{+0.57}_{-0.15}$	$4.63^{+2.60}_{-2.58}$	$0.48^{+0.24}_{-0.14}$	1*	$2.80^{+2.26}_{-1.81}$	$0.39^{+0.24}_{-0.13}$	1.25	96
CORE <sup>b</sup>	$0.33^{+0.33}_{-0.20}$	$0.47^{+0.15}_{-0.17}$	$0.93^{+3.73}_{-0.80}$	$7.29^{+28.0}_{-3.42}$	$2.18^{+0.71}_{-0.64}$	1*	$5.0^{+20.9}_{-3.5}$	$13.5^{+37.3}_{-8.2}$	$0.81^{+0.71}_{-0.49}$	1.56	14

**Note.** — (1) Foreground absorbing column density of the VMEKAL in units of  $10^{22} \text{ cm}^{-2}$ . (2) Temperature of component 1 in units of keV, where 1 represents the lower temperature component. (3) Normalization of component 1 in units of  $10^{-5} \int 10^{-14} n_e n_H dV / 4\pi D^2$ , where  $n_e$  is the electron number density,  $n_H$  is the hydrogen number density,  $V$  is the volume of plasma, and  $D$  is the distance between the sources and the observer. (4) Temperature of component 2 in units of keV, where 2 represent the higher temperature component. (5) Normalization of component 2, the units is the same with that of component 1. (6) O abundance in units of  $Z_\odot$ . (7) Mg abundance in units of  $Z_\odot$ . (8) Si abundance in units of  $Z_\odot$ . (9) Fe abundance in units of  $Z_\odot$ . (10) Reduced  $\chi^2$  of fit. (11) Degrees of freedom in the fit.

<sup>a</sup> Fitted spectrum in the energy range 0.4 – 3.0 keV.

<sup>b</sup> Fitted spectrum in the energy range 0.3 – 7.0 keV.

\* Denotes parameters held fixed.

**Table 2**  
The properties of plasma outflow in NGC 3628

Region	$R$ (1)	Component (2)	$kT$ (3)	$EI$ (4)	$n_e$ (5)	$M_{\text{plm}}$ (6)	$P_{\text{plm,thm}}$ (7)	$E_{\text{plm,thm}}$ (8)
HALO	6.72	1	0.21	6.07	$0.13 f^{-1/2}$	$40.0 f^{1/2}$	$0.09 f^{-1/2}$	$4.80 f^{1/2}$
		2	0.60	3.30	$0.09 f^{-1/2}$	$29.4 f^{1/2}$	$0.18 f^{-1/2}$	$10.1 f^{1/2}$
CORE	0.67	1	0.47	0.34	$0.95 f^{-1/2}$	$0.30 f^{1/2}$	$1.43 f^{-1/2}$	$0.08 f^{1/2}$
		2	7.29	1.55	$2.04 f^{-1/2}$	$0.64 f^{1/2}$	$47.7 f^{-1/2}$	$2.67 f^{1/2}$

**Note.** — (1) The radius of outflow in units of kpc. (2) The temperature component in absorbed two-temperature model, WABS\*(VMEKAL + VMEKAL), where 1 represents the lower temperature component, and 2 represent the higher temperature component. (3) Temperature in units of keV. (4) Emission Integral ( $EI = \int n_e n_H dV$ ) in units of  $10^{61} \text{ cm}^{-3}$ . (5) Number density in units of  $10^{-2} \text{ cm}^{-3}$ , where  $f$  is the filling factor. (6) Mass in units of  $10^6 M_\odot$ . (7) Thermal pressure in units of  $10^{-11} \text{ dyne cm}^{-2}$ . (8) Thermal energy in units of  $10^{55} \text{ erg}$ .

Nakai, N., Hayashi, M., Handa, T., et al. 1987, PASJ, 39, 685  
 Okumura, S. K., Momose, M., Kawaguchi, N., et al. 2000, PASJ, 52, 393  
 Rots, A. H. 1978, AJ, 83, 219  
 Sakamoto, K., Okumura, S., Minezaki, T., Kobayashi, Y., & Wada, K. 1995, AJ, 110, 2075  
 Sakamoto, K., Ho, P. T. P., Iono, D., et al. 2006, ApJ, 636, 685  
 Sakamoto, K., Ho, P. T. P., & Peck, A. B. 2006, ApJ, 644, 862  
 Sakamoto, K., Aalto, S., Wilner, D. J., et al. 2009, ApJ, 700, 104  
 Sanders, D. B., Mazzarella, J. M., Kim, D.-C., Surace, J. A., & Soifer, B. T. 2003, AJ, 126, 1607  
 Strickland, D. K., Colbert, E. J. M., & Heckman, T. M. 2001, ApJ, 560, 707  
 Strickland, D. K., Heckman, T. M., Weaver, K. A., Hoopes, C. G., & Dahlem, M. 2002, ApJ, 568, 689  
 Strickland, D. K., Heckman, T. M., Colbert, E. J. M., Hoopes, C. G., & Weaver, K. A. 2004, ApJ, 606, 829  
 Sunada, K., Kawabe, R., & Inatani, J. 1994, Int. J. Infrared Millimeter Waves, 14, 1251

Tsai, A.-L., Matsushita, S., Nakanishi, K., et al. 2009, PASJ, 61, 237  
 Tsutsumi, T., Morita, K.-I., & Umeyama, S. 1997, in ASP Conf. Ser. 125, Astronomical Data Analysis Software and Systems VI, ed. G. Hunt & H. E. Payne (San Francisco: ASP), 50  
 Tomisaka, K. & Ikeuchi, S. 1988, ApJ, 330, 695  
 Tully, R. B. 1988, *Nearby Galaxies Catalog* (Cambridge: Cambridge University Press)  
 Walter, F., Weiss, A., & Scoville, N. 2002, ApJ, 580L, 21W  
 Weaver, R., McCray, R., & Castor, J. 1977, ApJ, 218, 377  
 Weiss, A., Walter, F., Neininger, N., & Klein, U. 1999, A&A, 345, L23  
 Yokoo, T., Fukue, J., & Taniguchi, Y. 1993, PASJ, 45, 687  
 Young, J. S., & Scoville, N. Z. 1991, ARA&A, 29, 581